



HAL
open science

Photodegradation of ibuprofen using CeO₂ nanostructured materials: Reaction kinetics, modeling, and thermodynamics

Noemi Gallucci, Maryam Hmoudah, Eugénie Martinez, Amjad El-Qanni, Martino Di Serio, Luigi Paduano, Giuseppe Vitiello, Vincenzo Russo

► **To cite this version:**

Noemi Gallucci, Maryam Hmoudah, Eugénie Martinez, Amjad El-Qanni, Martino Di Serio, et al.. Photodegradation of ibuprofen using CeO₂ nanostructured materials: Reaction kinetics, modeling, and thermodynamics. *Journal of Environmental Chemical Engineering*, 2022, 10 (3), pp.107866. 10.1016/j.jece.2022.107866 . cea-04565951

HAL Id: cea-04565951

<https://cea.hal.science/cea-04565951>

Submitted on 3 May 2024

HAL is a multi-disciplinary open access archive for the deposit and dissemination of scientific research documents, whether they are published or not. The documents may come from teaching and research institutions in France or abroad, or from public or private research centers.

L'archive ouverte pluridisciplinaire **HAL**, est destinée au dépôt et à la diffusion de documents scientifiques de niveau recherche, publiés ou non, émanant des établissements d'enseignement et de recherche français ou étrangers, des laboratoires publics ou privés.

Photodegradation of Ibuprofen using CeO₂ Nanostructured Materials: Reaction Kinetics, Modeling, and Thermodynamics

Noemi Gallucci^{1,2}, Maryam Hmoudah^{1,3}, Eugenie Martinez⁴, Amjad El-Qanni³, Martino Di Serio¹,
Luigi Paduano^{1,2}, Giuseppe Vitiello^{2,5,*}, Vincenzo Russo^{1,6,*}

¹ *University of Naples Federico II, Department of Chemical Sciences, IT-80126 Naples, Italy.*

² *CSGI, Center for Colloid and Surface Science, IT-50019 Sesto Fiorentino (FI), Italy.*

³ *An-Najah National University, Department of Chemical Engineering, Nablus, Palestine.*

⁴ *University of Grenoble Alpes, CEA, LETI, F-38000 Grenoble, France.*

⁵ *University of Naples Federico II, Department of Chemical, Materials and Production Engineering, IT-80125 Naples, Italy.*

⁶ *Åbo Akademi, Laboratory of Industrial Chemistry and Reaction Engineering, FI-20500 Turku/Åbo.*

**corresponding authors: Giuseppe Vitiello (giuseppe.vitiello@unina.it) and Vincenzo Russo (v.russo@unina.it) at University of Naples Federico II.*

Abstract

Ibuprofen is one of the most used non-steroidal anti-inflammatory drugs, which is considered an emerging pollutant that may contaminate surface and underground water. Photodegradation using nanomaterials is one of the most sustainable and cheap technologies that can be used in water purification. In this study, the photodegradation efficiency of in-house prepared ceria (CeO_2) nanostructured materials towards ibuprofen was assessed under UV irradiation. CeO_2 nanoparticles (NPs) were prepared through wet-chemical synthesis and characterized by several techniques. The photodegradation activity of the synthesized CeO_2 -NPs was compared to the commercial Aeroxide TiO_2 -P25. Small crystalline CeO_2 -NPs were obtained with about 15 nm particle size, band-gap of 3.1 eV with irregular morphology. The surface area of CeO_2 -NPs was estimated to be $76 \pm 5 \text{ m}^2/\text{g}$. Dynamic light scattering analysis revealed that these nanoparticles have a strong tendency to self-aggregate and to form clusters in aqueous suspension. The results showed a slightly better performance of Aeroxide TiO_2 -P25 when compared to CeO_2 -NPs. On the other hand, five reusability tests confirmed the stability of CeO_2 -NPs in the adopted reaction conditions, without any significant effect on their photodegradation activity. The goodness of the kinetic modeling of the experimental data was proven through the estimated kinetic parameters, together with the statistical information. The temperature effect confirmed that the higher the temperature, the greater the dissociation rate. Thus, there is a direct relationship between temperature, reaction rate, and the activation energy for each reaction. Furthermore, the thermodynamic parameters, namely: the changes in Gibbs free energy (ΔG°), enthalpy (ΔH°), and entropy (ΔS°) have been reported revealing the efficient photodegradation performance of CeO_2 -NPs.

Keywords: Ibuprofen, CeO_2 nanoparticles, photodegradation, kinetic modeling, thermodynamics.

1. Introduction

Pharmaceutical compounds, such as ibuprofen, have received much attention recently due to their detection in water (surface and wastewater) and sediments [1]. Ibuprofen is considered one of the emerging pollutants that may contaminate surface and underground water due to the improper practices and disposal of unused medicine [2]. The presence of this compound in water bodies is considered problematic as many living beings can be adversely impacted due to the uncontrolled accumulation of these materials in the lipid tissues [3]. Numerous published studies and reviews about the occurrence, toxicity, and impact of ibuprofen were undertaken over the last few decades [4-7]. On one hand, this material is resistant to the available conventional treatment methods such as sedimentation, coagulation, filtration, and biological processes [3, 8]. On the other hand, most of the existing advanced wastewater treatment options such as distillation, membrane filtration, and electrochemical treatment are prohibitively expensive and face many operational challenges [9, 10]. Hence, photodegradation using nanomaterials is considered one of the state sustainable technologies that can be used in water purification [11-14]. This technology has many advantages because of the economic, environmentally friendly, simple, and easily operated designs needed to eliminate contaminants of emerging concern from water [15]. This will in turn improve drinking water quality and the safe reuse of water, thus protecting the environment, improving human health, and achieving sustainability goals [16].

Recently, cerium oxide has gained increasing attention for the degradation of organic contaminants in water [17-21]. In particular, a great interest has aroused the nanoparticles of cerium oxide nanoparticles (CeO_2 -NPs) because of their reactivity, reusability, cost-effectiveness, and environmental impact [22]. Based on the literature survey presented in Table 1, most of the published works on the application of CeO_2 -NPs solely in photodegradation focused on dyes, mainly on methylene blue. Therefore, paying attention to the photodegradation of emerging pollutants such as ibuprofen using CeO_2 -NPs is important in the field of water purification. Worth mentioning that the uniqueness of these nanoparticles lies in the simplicity of conversion between

Ce^{3+} and Ce^{4+} , the presence of defects, and the increase of the surface-to-volume ratio to the CeO_2 in bulk [23-25]. Moreover, Ce market price is around 4.57 – 4.71 \$/kg compared to 11.1 – 11.7 \$/kg for Ti [26], which oxides are nowadays considered as the most efficient photocatalysts [27, 28]. Thus, the use of CeO_2 could lead to a lower price of the catalyst.

In addition, CeO_2 is an n-type semiconductor with a band-gap at 3.1 eV [29], this wide band-gap of CeO_2 requires the use of UV light to activate the mechanism. To shift the band-gap from 3.1 to 2.45-2.90 eV and consequently use visible light for the photocatalytic activity, it is necessary to increase the number of defects in CeO_2 -NPs [30]. The photocatalytic activity of CeO_2 is closely linked to particle size, textural properties, and surface structure [31]. Therefore, an important parameter is the ratio $\text{Ce}^{3+}/\text{Ce}^{4+}$, which varies with the size of NPs that influence the photocatalytic activity. As Ce^{3+} switches to Ce^{4+} states, it results in high oxygen mobility in the CeO_2 lattice and in turn leads to a strong catalytic potential that happens without any structural modification of the fluorite lattice [30, 32]. The change in energy can cause largely a surface effect on catalyst [23]. Another important parameter determining the photocatalytic activity is the presence of oxygen vacancies in the lattice of CeO_2 , as the oxygen vacancies vary, consequently, the NPs properties vary [18, 20, 30, 33].

Herein, the synthesized CeO_2 -NPs have been tested under UV irradiation for the photodegradation of ibuprofen. The performance of these NPs was compared with Aeroxide TiO_2 -P25. Special attention was paid to the effect of air flow rate, stirring rate, temperature, catalyst bulk density, and ibuprofen solution initial concentration on the photodegradation efficiency of CeO_2 -NPs. Reusability, kinetics modeling, activation energy, and thermodynamics parameters were also addressed in this study.

Table 1. Some previous published works on the photocatalytic activity of CeO₂ nanoparticles in photodegradation.

Synthesis	Pollutant(s)	Radiation	Highlights	Reference
Co-precipitation method	Naphthol Blue Black dye	Sunlight	<ul style="list-style-type: none">CeO₂ has a low activity for the degradation of naphthol blue black dye. Dopping with Mn, showed increased photocatalytic activity.	[21]
Electron beam accelerator was used to modify pristine CeO ₂	4-nitrophenol and methylene blue	Visible-light	<ul style="list-style-type: none">EB can effectively narrow the band gap of metal oxides for the enhanced visible light photocatalytic activities.	[30]
Solvothermal method	Phenol and its derivatives (2-chlorophenol, 2-bromophenol and 2-nitrophenol)	Sunlight	<ul style="list-style-type: none">The interaction of UV photons induced defects at the surface of CeO₂.	[20]
Precipitation method	Methyl orange and methylene blue	UV-light	<ul style="list-style-type: none">CeO₂ nanoparticles showed moderate degradation rate in comparison with other metal oxide-based nanoparticles.	[19]
Green synthesis using leaf extract of <i>Azadirachta indica</i> plant	Rhodamine B dye	UV-light	<ul style="list-style-type: none">Excellent photocatalytic activity of green CeO₂ nanoparticles towards RhB dye.	[34]
Hydrothermal method	Isopropyl alcohol	Visible-light	<ul style="list-style-type: none">Confeito-like CeO₂ exhibits excellent performance for the decomposition of isopropyl alcohol to acetone.Ce³⁺ induced oxygen vacancies in the lattice of CeO_{2-x}, and this resulted in an improvement in the activity.	[18]
Wet chemical method	Congo red and methyl orange	Visible-light	<ul style="list-style-type: none">CeO₂ nanocubes showed high reactivity and stability for the photodegradation of dyes	[35]
Sonochemical-assisted method	Methylene blue	UV-light	<ul style="list-style-type: none">After 75 min of radiation, 85% of methylene blue were degraded.	[17]
Hydrothermal method	Methylene blue	Under dark, sunlight, and UV irradiation	<ul style="list-style-type: none">The performance varied based on the surface areas, nanoparticles shape and the content of oxygen vacancies.	[36]

Solution combustion technique	Methylene blue	UV-light	<ul style="list-style-type: none"> The photocatalytic performance was optimised in terms of solution pH, catalyst dose, initial methylene blue, and UV irradiation time. 	[37]
Commercial CeO ₂ nanoparticles	Tropaeolin O	UV-light	<ul style="list-style-type: none"> Effect of the particle size and pH were investigated. The degradation of Tropaeolin O was confirmed by toxicity experiments in the presence of CeO₂ NPs and marine crustaceans as <i>A. salina</i>. 	[38]

2. Materials and methods

2.1 Materials

Ibuprofen solutions were prepared using 4-isobutyl- α -methylphenylacetic acid at 99% (Alfa Aesar). Cerium (III) nitrate hexahydrate salt ($\text{Ce}(\text{NO}_3)_3 \cdot 6\text{H}_2\text{O}$, purity >99.999%), ammonia solution 30 v/v%, and hydrogen peroxide were purchased by Sigma-Aldrich (Milan, Italy). Bi-distilled Milli-Q water, also filtered using 0.20 μm filters, was obtained through Merck Millipore (Darmstadt, Germany). Commercial Aeroxide TiO_2 -P25 was supplied by Evonik Industries (Essen, Germany) for comparative purposes in this study. All materials were used without any further treatment.

2.2 Methods

2.2.1 Synthesis of CeO_2 nanoparticles

Typically, CeO_2 -NPs were prepared through a wet-chemistry synthesis in solvothermal conditions, according to reference [39]. First, 30 mL of an aqueous solution (0.5 M) of $\text{Ce}(\text{NO}_3)_3 \cdot 6\text{H}_2\text{O}$ salt was prepared and left under magnetic stirring for 10 minutes to induce a complete salt dissolution. Subsequently, 117 μL of hydrogen peroxide was added to the Ce(III) salt solution which was stirred for 5 minutes to favor the oxidation of Ce^{3+} to Ce^{4+} . A specific volume (~ 6 mL) of a diluted ammonia solution (7 M) was then added to this mixture until a pH of 8.8 to start the precipitation reaction. Afterward, the mixture was continuously stirred at 80 $^\circ\text{C}$ for 1 h to complete the reaction. After an hour, a yellow precipitate constituted by $\text{Ce}(\text{OH})_4$ was obtained and washed three times with bi-distilled Milli-Q water by centrifugation at 9000 rpm for 10 minutes. The pH was adjusted to pH 10 by using the ammonia solution and 30 mL of washed precipitate were treated at 120 $^\circ\text{C}$ for 24 hours within a mini-reactor. The final CeO_2 -NPs were repeatedly washed with bi-distilled Milli-Q water by centrifugation at 9000 rpm for 10 minutes.

2.2.2 Physico-chemical characterization

X-Ray Diffraction (XRD) analysis. XRD measurements were performed by a PANalytical diffractometer (Malvern, Worcestershire, United Kingdom) with a nickel filter and $\text{CuK}\alpha$ radiation,

with a step size of 0.02° and a counting time of 80 s per step, to investigate the formation and the properties of CeO_2 crystalline phases. The average crystal size (τ) was evaluated through the Scherrer formula:

$$\tau = \frac{K\lambda}{\beta \cos\theta} \quad (1)$$

where τ is the mean size of the crystallite domains, K is a dimensionless shape factor, λ is the X-ray wavelength, β is the broadening at half the maximum intensity (FWHM), θ is the Bragg angle.

X-ray photoelectron spectroscopy (XPS). Surface properties of CeO_2 -NPs were investigated by XPS analyses which were carried out using a spectrometer VersaProbe II with a monochromatic Al K α X-ray source ($h\nu=1486,6$ eV), a spot of 200 μm , and a dual-beam system (Ar^+ et \bar{e}) for charge compensation. The pass energy was set at 23.5 eV, leading to an overall energy resolution of 0.6 eV. Photoelectrons were collected at a take-off angle of 45° , which means a sampling depth of approximately 5 nm. The relative atomic composition (% at.) is given with an uncertainty of $\pm 20\%$ using tabulated relative sensitivity factors. Decomposition of the spectra was done using Voigt functions after Shirley's background subtraction with the Multipak software.

Transmission Electron Microscope (TEM). Morphological properties of CeO_2 -NPs were investigated by TEM. The analyzed sample was prepared by placing 10 μL of nanoparticles suspension on one side of a 200-mesh carbon-coated copper grid which was allowed to dry in air. TEM images were obtained by FEI TECNAI G2 200kV microscope (ThermoFisher Scientific, Waltham, USA) equipped with a high-angle annular dark-field (HAADF) detector for high-resolution imaging.

Dynamic Light Scattering (DLS). DLS measurements were performed to measure the size of CeO_2 -NPs in an aqueous environment with a home-made instrument composed of a Photocor compact goniometer (Moscow, Russia), SMD 6000 Laser Quantum 50 mW light source (Laser Quantum, Fremont, CA, USA) operating at 532.5 \AA , a photomultiplier (PMT-120-OP/B) and a correlator (Flex02-01D) from Correlator.com (Shenzhen, China). The experiments were carried out on 1mL of

an aqueous suspension of CeO₂-NPs at the constant temperature (25.0 ± 0.1) °C, by using a thermostatic bath and at the scattering angle θ of 90°. The scattered intensity correlation function was analyzed using a regularization algorithm. The diffusion coefficient of each population of particles was calculated as the z-average of the diffusion coefficients of corresponding distributions.

Surface area and porosimeter analysis. The specific surface area (S_{BET}) and the pore volume (V_{P}) of CeO₂-NPs were evaluated by generating seven-point isotherms at 77 K for N₂ adsorption (Autosorb-1, Quantachrome) using a particular amount of the sample capable of providing a specific surface area equal to 5 m² in the sample cell. The mesopore volume (V_{BJH}), the average pore radius (r_{p}), and the pore size distributions were estimated by the Barreto– Joyner–Halenda (BJH) method applied to the desorption branch of the isotherm [40].

Ultra-violet and visible light diffuse reflection (UV-Vis DRS) spectroscopy. UV-Vis DRS measurements on powdered CeO₂-NPs were carried out using a UV-2600i UV-VIS spectrophotometer, 230V (Shimadzu, Milan, Italy), equipped with an integrating sphere ISR-2600Plus operating in a wavelength range of 220 - 1400 nm. Barium sulfate was exploited as a reflectance standard. The measured intensity was expressed as the value of the Kubelka–Munk function $F(R)$, while the band-gap value was evaluated by linearization of the plot of $(F(R)h\nu)^{1/2}$ against $h\nu$.

High Pressure Liquid Chromatography (HPLC). Ibuprofen concentration analyses were carried out using an Agilent 1100 High Pressure Liquid Chromatography (HPLC) system, with a 70% w/w methanol, 30% w/w water mobile phase. The column used was a Phenomenex Luna C18, with a 5 μ m particle size, 100 Å pore size, 250 mm length, and 4.6 mm internal diameter. The detector used was a Diode Array Detector (DAD), with a 1024-element photodiode array, deuterium, and tungsten lamps with a 190-950 nm wavelength range. The software used for apparatus control and data collection was Agilent Chemstation. This system acquires the absorbance of the eluates in

mAU (Absorbance Units) as a function of elution time in the whole emission interval of the lamps and outputs a 3D chromatogram with X elution time, Y wavelength, and Z signal intensity.

2.2.3 Photodegradation experimental set-up

Photodegradation experiments were conducted in a 1.5 L jacketed glass vessel, equipped with a three-neck head. The reactor was connected to an ultra-thermostat to regulate the temperature at the desired level. The liquid temperature was monitored with a dedicated thermocouple. Air was fed to the reactor system using a digital flow-meter regulator (supplied by Bronkhorst), connected to a sintered filter used as a gas sparger, to provide a good gas-liquid interface in the mass transfer of air to the liquid phase. A coaxial 4W UV lamp was mounted at the center of the reactor (Toshiba FL4BLB), characterized by a wavelength of $\lambda = 365$ nm, with dimensions of 15 cm \times 1.5 cm. The liquid was stirred by a magnetic impeller at the desired rate.

In the classical execution of the experiment, ibuprofen solution was prepared with the desired concentration and was then loaded into the reactor and stirred at the set value. The reactor was closed with the lid and connected to the thermostat, set at a pre-specified reaction temperature. Airflow was adjusted with a pressure reducer to 1 bar and the digital flow meter was set at a fixed flow. At this point, the catalyst was loaded into the reactor. The reactor was then shielded before switching on the UV lamp to reduce any ray dispersion, avoiding any risks to the operator. A first sample was collected to measure the ibuprofen concentration (time = 0 sample). The reaction was then started by switching on the lamp, withdrawing samples periodically to follow the reaction kinetics until a maximum time of 5h. Each sample was then centrifuged at 3300 rpm for 30 minutes, and the resulting liquid sample was analyzed by UV-VIS spectroscopy (UV-Vis Jasco V-550). A classical spectrum was reported in the supplementary material (Figure S.1). A calibration curve was built at $\lambda = 222$ nm, where ibuprofen absorption reached the maximum value, obtaining the calibration curve reported in Eq. 2, valid in a concentration range between 0.0 – 0.05 mol/m³ (Figure S.2).

$$c_{IBU} = (0.113 \pm 0.001) Abs, R^2 = 0.99 \quad (2)$$

where Abs represents the absorbance and c_{IBU} is the ibuprofen concentration expressed in mol/m^3 .

To investigate the reaction kinetics, together with eventual mass transfer limitations, several experiments were conducted by varying the operational conditions in a wide range. The summary of the adopted reaction conditions is reported in Table S.1.

2.2.3 Modeling and parameter estimation

Matlab R2020b was used to conduct all the modeling activities reported in the present work. Ordinary differential equations were solved using *ode23s* routine, while parameter estimation activity with *particleswarm* algorithm. The objective function was calculated as follows [31]:

$$F_{obj} = \frac{1}{N_{data}} \sqrt{\sum_{i=1}^{N_{data}} \left(\frac{c_{i,EXP} - c_{i,CALC}}{c_{i,EXP}} \right)^2} \quad (3)$$

Confidence intervals were calculated using *nlparci* algorithm.

3. Results and discussion

3.1 Physico-chemical features of synthesized CeO₂ nanoparticles

Characterization of CeO₂ NPs was carried out using XRD and XPS measurements. XRD pattern of CeO₂-NPs, shown in Figure 1, indicated the presence of the typical peaks of a face-centered cubic (FCC) structure (JCPDS no81-0792) [31, 41, 42]. The peaks obtained at the diffraction angles (2θ) of 29°, 33°, 47°, 56°, and 59° correspond to the Miller indices (hkl) indicating the crystalline planes (111), (200), (220), (311) and (222) respectively, as shown in Figure 1, and confirming the formation of CeO₂ nanoparticles with a fluorite-type crystalline structure. The mean crystallite sizes estimated from Scherrer's formula were close to 18 ± 1 nm. Then, XPS analysis was performed to obtain information concerning the chemical composition of the surface of the CeO₂ nanoparticles. The survey spectrum is plotted in Figure 2A, showing the main characteristic peaks of CeO₂ (Ce 3d, Ce 4d and O1s) as well as carbon contamination (C 1s). A zoom on the oxygen O1s core level is presented in the inset, highlighting two contributions related to O-Ce bonds from the CeO₂ NPs and O-C bonds from hydrocarbon surface contamination. The spectrum of the Ce 3d core level is reported in Figure 2B. This spectrum exhibits strong satellite features (cf^1L) to the main peaks (cf^0). For each component of the Ce 3d_{5/2} - Ce 3d_{3/2} doublet, 5 peaks were used to fit all these contributions, each of them being assigned to one of the Ce oxidation states (Ce³⁺ and Ce⁴⁺) as indicated in Table S.2. The Ce³⁺/Ce⁴⁺ ratio was estimated to be equal to 0.4, as deduced from the areas of these different components.

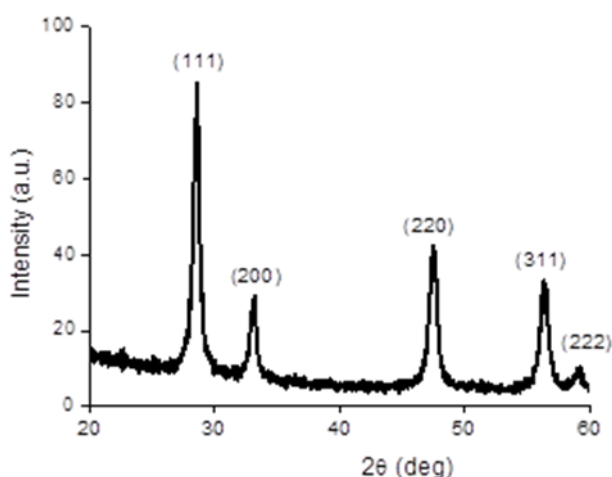


Figure 1. XRD pattern of the CeO₂ NPs.

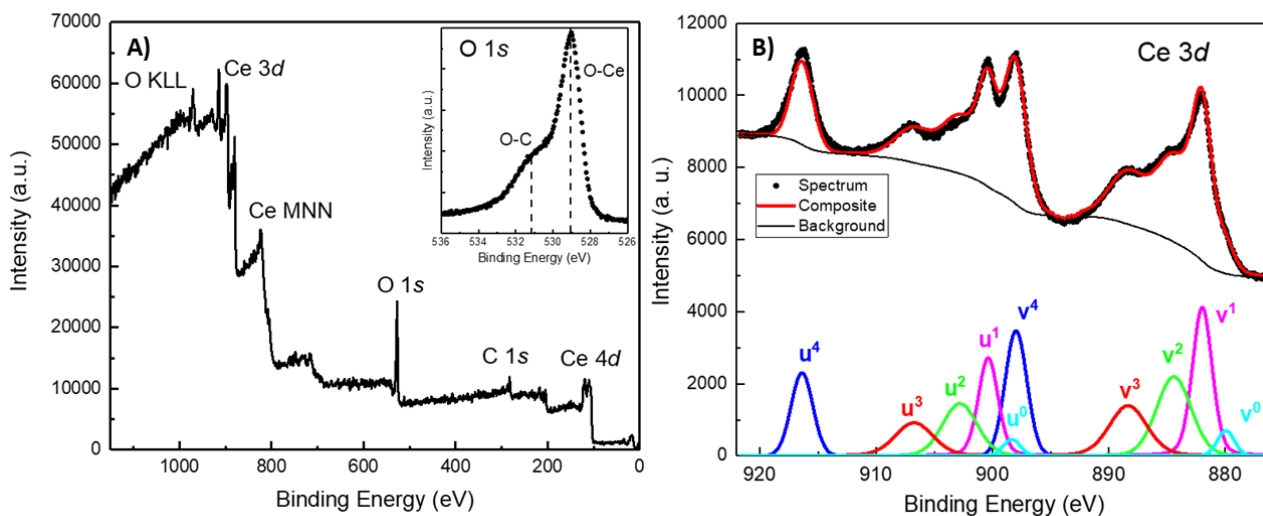


Figure 2. A) XPS survey scan and O 1s spectrum B) Ce 3d XPS spectrum of the CeO₂ NPs.

Morphological and textural features of CeO₂-NPs were analyzed by TEM (Figure 2A). In particular, a representative TEM image shows the formation of small nanoparticles of about 15 nm in size and with irregular morphology. At the same time, it suggests a strong tendency of these nanoparticles to self-aggregate forming clusters with a size comparable to that obtained through DLS analysis (Figure 2B). As observed from the hydrodynamic radius distribution, the main population is centered at about 530 ± 70 nm confirming a fast and significant self-aggregation of bare CeO₂ nanoparticles when they were in an aqueous suspension. In addition, S_{BET} of CeO₂-NPs was measured by N₂ adsorption at 77K and the estimated surface area was equal to 76 ± 5 m²/g. The adsorption/desorption isotherm shows a type IV-hysteresis, which is typical of porous materials (see Figure S.3). Size distribution of pores was estimated according to the BJH model based on the desorption branch of the isotherm, indicating that the total volume of the pores is equal to 0.22 cm³/g, while the pore distribution (as derivative of the pore volume to the radius) shows the presence of a single population of pores with a diameter of 1.35 ± 0.15 nm.

Moreover, the optical properties of CeO₂-NPs at solid-state were also investigated by recording the DRS spectrum, displayed in Figure 2C. The measured intensity was expressed as the value of the Kubelka-Munk function $F(R)$ (see Figure 2C) which indicates an absorption at $\lambda < 300$ nm. The optical band-gap for the transition from the valence band (V_B) to the conduction band (C_B) was calculated by linearization of the plot of $(F(R)h\nu)^{1/2}$ against photon energy (as shown in Figure 2D) and was equal to 3.1 eV, in agreement with the literature which reports a strikingly dependence on the preparation method [43].

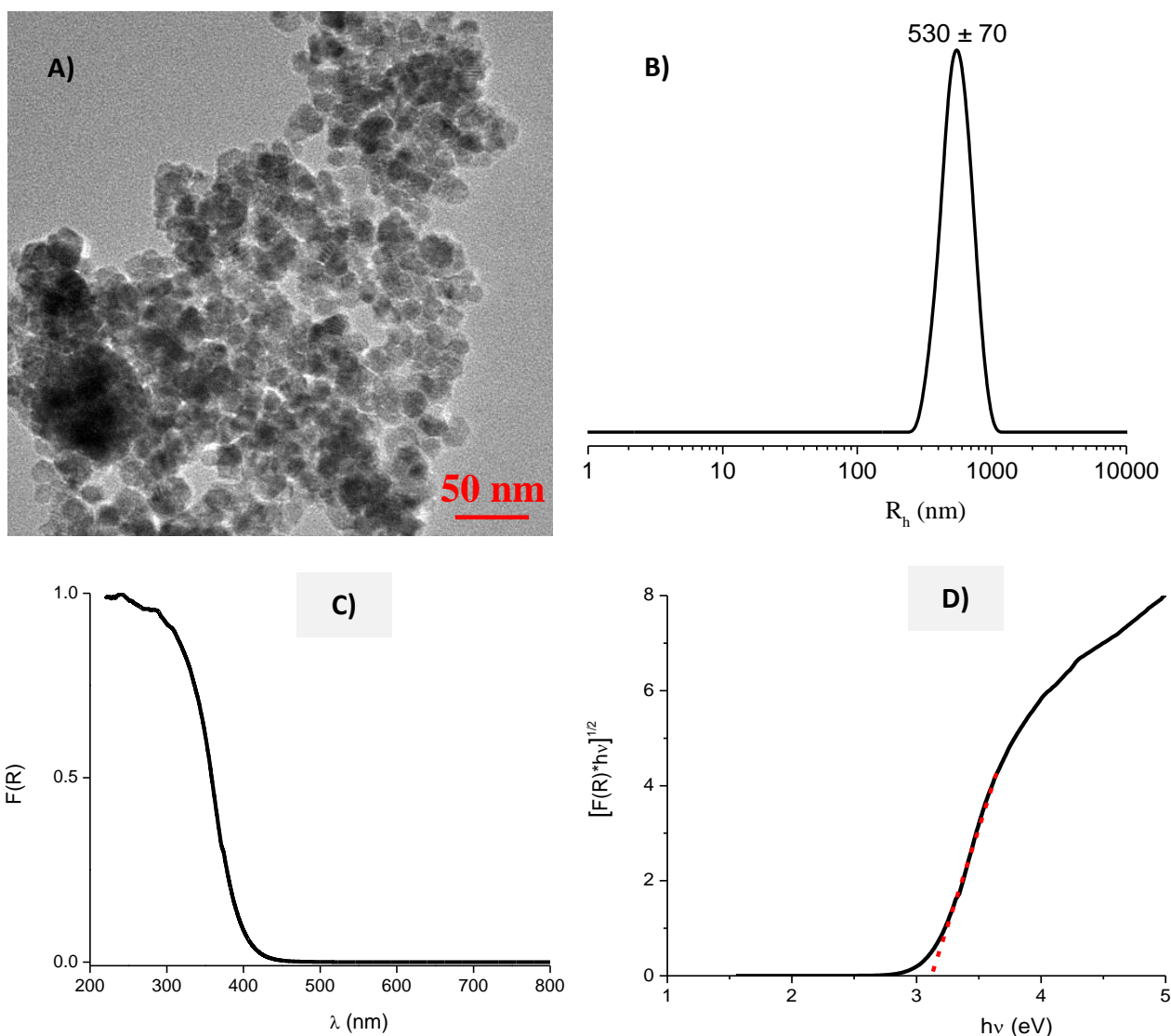


Figure 2. A) TEM image, B) hydrodynamic radius distribution of CeO₂ NPs in the aqueous medium, C) UV-DRS spectrum of powdered CeO₂-NPs, and D) estimation of the optical band-gap using the modified Kubelka-Munk function.

3.2 Photodegradation experimental results

A first experiment was conducted in the absence of the catalyst, to verify eventual photodegradation due to the UV irradiation (Figure S.4). As revealed, a maximum conversion was observed to be 5%, reaching a stable plateau value. This concludes that ibuprofen can be considered rather stable under UV light. A second blank experiment was conducted by putting in contact the ibuprofen solution with CeO₂ nanoparticles, in the absence of UV irradiation. In this case, no ibuprofen adsorption was observed, probably due to the slightly big dimension of ibuprofen compared to the catalyst pores.

Further, the synthesized material was compared with Aeroxide TiO₂-P25, considered nowadays as a benchmark catalyst for photodegradation studies. Considering the fixed operation conditions, Aeroxide TiO₂-P25 shows slightly better performance compared to CeO₂ (Figure 3A). This encouraging result proves the novelty of these nanomaterials that can be attributed to their lower band-gap value (2.95 eV against 3.30 eV of TiO₂-P25), thus, considered promising in an eventual industrial application. Before investigating the reaction kinetics, the catalyst was recovered from the experiment and reused for 5 times, to check the catalyst stability. The results are reported in Figure 3B, showing good stability as well as recyclability in the adopted reaction conditions.

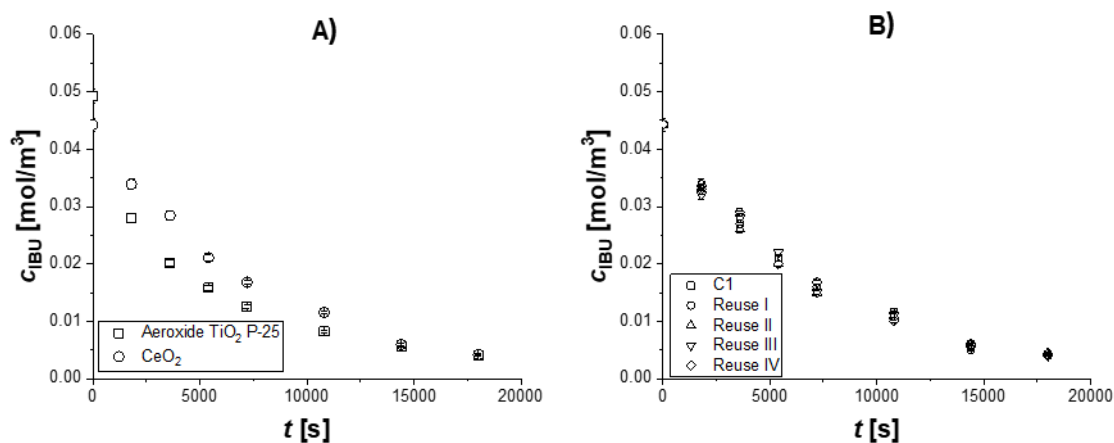


Figure 3.
A) Comparison between Aeroxide

TiO₂-P25 and CeO₂-NPs towards ibuprofen photodegradation. Adopted reaction conditions: $T = 303$ K, $c_{IBU,0} = 5 \cdot 10^{-2}$ mol/m³, $\rho_B = 0.37$ kg/m³, $\nu = 750$ rpm, UV irradiation. **B)** Reuse tests' results, in terms of ibuprofen concentration vs the reaction time for different reuses. Experimental conditions: $T = 303$ K, $c_{IBU,0} = 5 \cdot 10^{-2}$ mol/m³, $\rho_B = 0.37$ kg/m³, $Q_{air} = 1.0 \cdot 10^{-6}$ m³/s, and $\nu = 750$ rpm.

Different experiments were conducted to check the influence of both gas-liquid and liquid-solid mass transfer resistances. In particular, the airflow fed to the reactor was varied to verify if the gas-liquid mass transfer could affect the overall rate of the reaction network (Figure S.5). It can be concluded that by increasing the airflow, an increase in the reaction rate can be observed, reaching a stable plateau at $1.0 \cdot 10^{-6}$ m³/s of airflow, confirming that gas-liquid mass transfer resistance can be neglected. Thus, all the other experiments were conducted imposing $1.0 \cdot 10^{-6}$ m³/s airflow.

The impeller rate was varied in a range of 250 – 750 rpm to detect the optimal stirring rate to avoid fluid-solid mass transfer limitation (see Figure S.6). It was found that beyond 500 rpm, a stable reaction rate was measured. Thus, the kinetics investigation was conducted imposing an optimal stirring rate of 750 rpm.

The influence of the reaction temperature was also investigated, as shown in Figure 4. It is noted that by increasing the reaction temperature, an increase in the reaction conversion can be observed. When analyzing the samples, a second absorption peak was noticed at $\lambda = 260$ nm, corresponding to 1-OXO ibuprofen, the most probable by-product that can be formed [44]. This compound was verified by HPLC mass analysis. No further by-products were detected neither by HPLC mass nor by UV-Vis. Probably, further photodegradation products would be formed at longer reaction times of harsh reaction conditions. The by-product concentration evolution with temperature follows a logical trend, showing an increase in the initial formation rate with temperature, passing then through a maximum due to its further photodegradation.

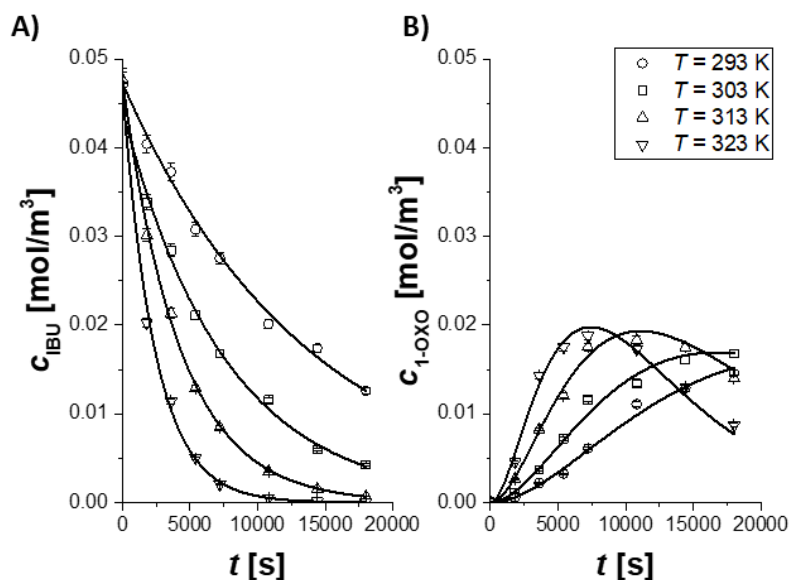


Figure 4. Experimental results of the kinetic tests conducted at different temperatures, fixing $c_{IBU,0} = 5 \cdot 10^{-2} \text{ mol/m}^3$, $\rho_B = 0.37 \text{ kg/m}^3$, $Q_{air} = 1.0 \cdot 10^{-6} \text{ m}^3/\text{s}$ and $v = 750 \text{ rpm}$. Trends of the concentration profiles vs the reaction time for A) ibuprofen and B) 1-OXO ibuprofen. Lines are the calculated profiles. The subplots refer to the same legend.

The influence of the catalyst loading on the reaction rate was investigated by conducting experiments using different catalyst bulk densities. Figure 5 shows that by increasing the catalyst concentration, an increase of ibuprofen photodegradation was measured. Even the by-product shows a higher consumption after a higher rate of formation.

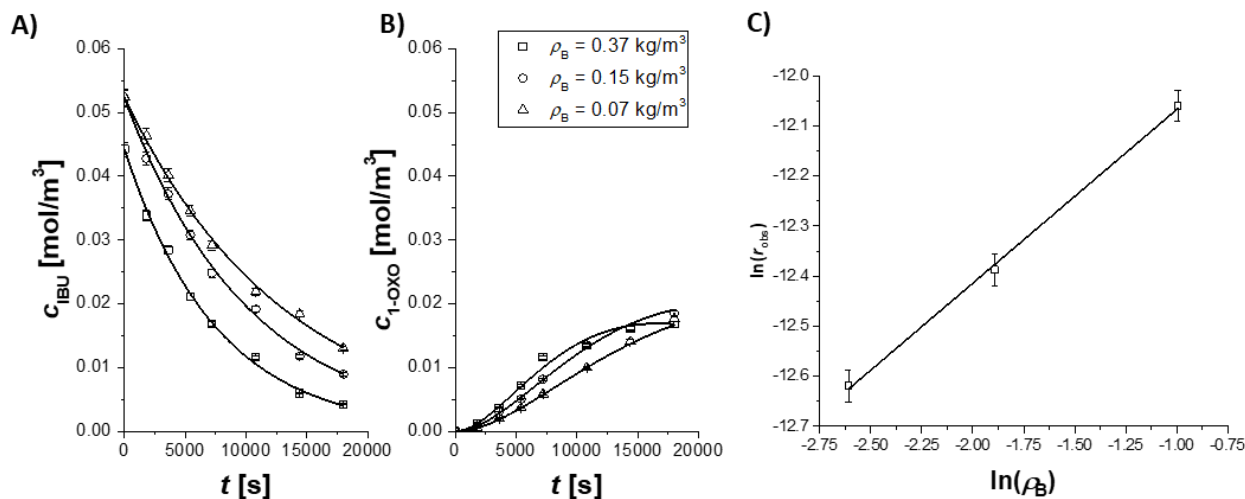


Figure 5. Experimental results of the kinetic tests conducted at different catalyst loading, fixing $c_{IBU,0} = 5 \cdot 10^{-2} \text{ mol/m}^3$, $T = 303 \text{ K}$, $Q_{air} = 1.0 \cdot 10^{-6} \text{ m}^3/\text{s}$ and $v = 750 \text{ rpm}$. Trends of the concentration profiles vs the reaction time for **A)** ibuprofen and **B)** 1-OXO ibuprofen. Lines are the calculated profiles. The subplots refer to the same legend. The panel **C)** represents catalyst bulk density linearization test.

Finally, three different experiments were conducted varying the initial ibuprofen concentration, to verify the reaction order (Figure 6). The results show that the higher the initial content of the contaminant, the faster is the reaction rate, suggesting a first-order reaction. This aspect will be better described and discussed in the following experimental data kinetics modeling section. The same behavior was observed for 1-OXO ibuprofen, suggesting a higher formation rate when a more concentrated solution of contaminant is used.

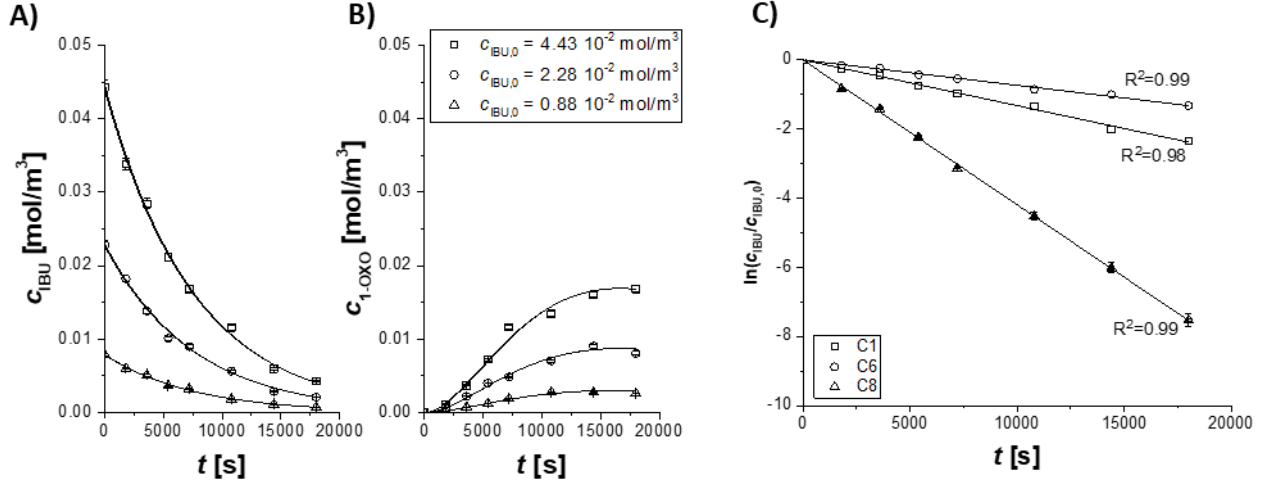


Figure 6. Experimental results of the kinetic tests conducted at different initial ibuprofen concentrations, fixing $T = 303 \text{ K}$, $\rho_B = 0.37 \text{ kg/m}^3$, $Q_{air} = 1.0 \cdot 10^{-6} \text{ m}^3/\text{s}$ and $v = 750 \text{ rpm}$. Trends of the concentration profiles vs the reaction time for **A)** ibuprofen and **B)** 1-OXO ibuprofen. Lines are the calculated profiles. The subplots refer to the same legend. The panel **C)** represents first-order linearization test.

3.3 Kinetics modeling

To interpret the kinetics data, several assumptions must be made based on the experimental observations. First, as only ibuprofen and 1-OXO ibuprofen were detected, an in-series reaction mechanism was proposed, passing through the formation of 1-OH ibuprofen [45]. Thus, the following reaction mechanism was imposed:



Each elementary step was considered of a first-order for oxygen, taken at saturation. No adsorption was considered as the concentrations of both reactant and products are rather low. This assumption was confirmed by simple linearization, where $\ln(c_{IBU}/c_{IBU,0})$ was plotted vs the experimental time, as demonstrated in Eq. 4.

$$\frac{dc_{IBU}}{dt} = -r \rho_B^n \rightarrow \frac{dc_{IBU}}{dt} = -k c_{IBU} \rho_B^n \rightarrow \int_{c_{IBU,0}}^{c_{IBU}} \frac{dc_{IBU}}{c_{IBU}} = \int_0^t -k \rho_B^n dt \rightarrow \ln \left(\frac{c_{IBU}}{c_{IBU,0}} \right) = -k \rho_B^n t \tag{4}$$

Data are aligned to a straight line, as revealed previously in Figure 6C, demonstrating that the reaction kinetics follow a first-order rate law.

Oxygen concentration was considered varying with temperature, imposing the following empirical equation fitted on data published in the literature [39], ensuring the right oxygen concentration calculated at the temperature chosen for each experiment, Eq. 5.

$$c_{O_2} = (52.94 \exp(-T / 25.9) + 7.5 \cdot 10^{-4}) \rho_{H_2O} \quad (5)$$

The experimental data were interpreted with a pseudo-homogeneous single-phase model, as neither fluid-solid nor intraparticle diffusion limitations, from the results reported in the previous section. In particular, the Weisz-Prater criterion was calculated to be sure that intraparticle limitations were absent, but as particles were rather small (500 nm aggregates), this result suggests that no diffusion limitations affect the reaction kinetics. The general mass balance equation that was adopted is reported in Eq. 6.

$$\frac{dc_i}{dt} = \sum_{j=1}^{N_r} \nu_{ij} r_j \rho_B^n \quad (6)$$

The catalyst bulk density was elevated to a proportional coefficient n , to take into consideration the shielding effect of the catalyst loading on the UV-light penetration in the liquid phase [41]. This coefficient can be calculated directly from the experimental data, plotting the $\ln(r_{obs})$ vs $\ln(\rho_B)$, as in Eq. 7.

$$r_{obs} = r \rho_B^n \rightarrow \ln(r_{obs}) = \ln(r) + n \ln(\rho_B) \quad (7)$$

It is observed that the data are linear in Figure 5C and the calculated coefficient is $n = 0.35 \pm 0.01$. A parameter estimation analysis was conducted simultaneously on C1, C6-C10 (Table S.1), to retrieve kinetics information, the kinetics constant was calculated at a reference temperature $T_{ref} = 303$ K, and activation energy for each reaction, adopting the modified Arrhenius equation reported in Eq. 8.

$$k_j = k_{ref,j} \exp\left(\frac{-Ea_j}{R} \left(\frac{1}{T} - \frac{1}{T_{ref}}\right)\right) \quad (8)$$

The summary of the obtained parameters, together with statistical information are reported in Table 2, while the obtained fits are presented earlier in Figures 4 – 6.

Table 2. Summary of the estimated kinetic parameters, together with statistical information. $T_{ref} = 303$ K, CI 95% represent the confidence interval at 95%, M the correlation matrix.

Parameter	Value \pm CI 95%	Units	%Error	M	$k_{ref,1}$	Ea_1	$k_{ref,2}$	Ea_2	$k_{ref,2}$	Ea_3
$k_{ref,1}$	$(1.59 \pm 0.05) \cdot 10^{-4}$	$(m^3/mol)(m^3/kg^n)s^{-1}$	1.3	$k_{ref,1}$	1.0					
Ea_1	55.8 ± 0.6	kJ/mol	1.0	Ea_1	-0.2	1.0				
$k_{ref,2}$	$(2.01 \pm 0.11) \cdot 10^{-4}$	$(m^3/mol)(m^3/kg^n)s^{-1}$	5.5	$k_{ref,2}$	-0.2	0.1	1.0			
Ea_2	29 ± 3	kJ/mol	11.8	Ea_2	0.1	-0.1	-0.6	1.0		
$k_{ref,3}$	$(1.08 \pm 0.07) \cdot 10^{-4}$	$(m^3/mol)(m^3/kg^n)s^{-1}$	6.1	$k_{ref,3}$	0.1	-0.1	0.7	-0.5	1.0	
Ea_3	31 ± 3	kJ/mol	10.6	Ea_3	-0.1	0.1	-0.6	0.5	-0.8	1.0

The calculated activation energies presented in Table 2 are all within a range of kinetics regime. The three constants are of the same order of magnitude; thus, no rate-determining step can be assumed among the involved reactions. The calculated errors on all the kinetic parameters are below 12%. Only a slight correlation can be seen among the parameters. Hence, from Figures 4 – 6 it is evident that the fit can be considered more than acceptable, confirming the goodness of the made assumptions.

3.4 Thermodynamics analysis

The effect of different temperatures, i.e., 293, 303, 313, and 323 K on ibuprofen photodegradation using CeO_2 -NPs was investigated. Table 3 summarizes the obtained rate constants and the corresponding values of the thermodynamic parameters namely; ΔG° , ΔH° , and ΔS° . It can be observed that increasing the reaction temperature, increases the rate constants and the

corresponding photodegradation efficiency. This was previously confirmed in Figure 4 and in the kinetics modeling section where the probability of collisions increases yielding into enhancing the photodegradation efficiency [46]. To estimate the thermodynamic parameters, equations 9 – 11 were used.

$$\Delta H^\circ = E_a + RT$$

$$(9) \quad \ln(k/T) = \ln(K_B/h) + (\Delta S^\circ/R) - (\Delta H^\circ/RT)$$

$$(10)$$

$$\Delta G^\circ = \Delta H^\circ - T\Delta S^\circ$$

$$(11)$$

where, ΔG° is the activation Gibbs free energy, ΔH° the change in enthalpy, ΔS° is the change in entropy, R is the ideal gas constant (8.314 J/mol.K), K_B is Boltzmann constant (1.38×10^{-23} m².kg/s².K), h Plank constant (6.63×10^{-34} m².kg/s), k is the kinetics rate constant (m³/mol)s⁻¹.

Table 3. Kinetic and thermodynamic parameters for the photodegradation of ibuprofen using CeO₂-NPs at $E_{a1} = 55.8$ kJ/mol.

T (K)	k (m ³ /mol)s ⁻¹	$\ln(k/T)$	$\Delta H^\circ/RT$	ΔH° (kJ.mol ⁻¹)	ΔS° (kJ.mol ⁻¹ K ⁻¹)	ΔG° (kJ.mol ⁻¹)
293	2.7×10^{-5}	-16.18	23.91	58.2	0.55	42.1
303	5.9×10^{-5}	-15.45	23.15	58.3		41.6
313	1.2×10^{-4}	-14.78	22.44	58.4		41.1
323	2.3×10^{-4}	-14.15	21.78	58.5		40.7

The relatively high positive values of ΔG° and ΔH° designate the endothermic non-spontaneous reaction forming a highly hydrated transition state complex with weak bonds for rapid degradation of the activated complex [46-48]. The values of ΔG° decreased with increasing the temperature, which means that the spontaneity of photodegradation is proportional to temperature. Moreover, the positive value of ΔS° suggests that the system exhibits a random behavior that supports a higher degree of degradation of ibuprofen into simple products [46].

4. Conclusions

This work investigates the ability of CeO₂ nanostructured materials, obtained through the wet-chemical approach, in exerting a notable photodegradation of ibuprofen. The synthesis strategy led to the successful preparation of small crystalline CeO₂-NPs with a size of about 15 nm and a band-gap of 3.1 eV against which the synthesized material showed a comparable photocatalytic activity. BET surface area of the prepared CeO₂-NPs was estimated to be around 76 ± 5 m²/g with a strong tendency to self-aggregate and to form clusters in aqueous suspension as confirmed by TEM and DLS analysis. XPS analysis was performed to gain a deeper insight into the chemical composition of the surface of the CeO₂-NPs, where the ratio of Ce³⁺/Ce⁴⁺ was estimated to be 0.4, as deduced from the areas of these different components. It was found that an increase in the reaction rate reaches a plateau at $1.0 \cdot 10^{-6}$ m³/s when increasing the airflow which in turn proves that gas-liquid mass transfer resistance can be neglected. A stable reaction rate was measured starting from 500 rpm and the kinetic reaction experiments were accordingly conducted at 750 rpm. The corresponding reaction conversion increased when increasing the reaction temperature. The reusability of the CeO₂-NPs study indicated that they can be used repeatedly, without impacting their capacity, confirming their sustainability. It is worth mentioning, that CeO₂-NPs show similar activity to the commercial TiO₂-P25, hence the use of Ce can be more convenient when considering its market price that is lower than Ti. For the kinetics modeling, the experimental data were interpreted with a pseudo-homogeneous single-phase model, suggesting that no diffusion limitations affect the reaction kinetics. The calculated activation energies were all within a range of kinetic regime with no rate-determining step among the involved reactions. The thermodynamic parameters of the photodegradation of ibuprofen have been reported. The relatively high positive

values of ΔG° and ΔH° indicate the endothermic and non-spontaneous nature of the reaction forming a highly hydrated transition state complex with weak bonds for rapid degradation of the activated complex. While the positive value of ΔS° suggests that the system exhibits a random behavior with enhanced photodegradation performance of CeO₂ NPs towards ibuprofen. Overall, the findings promote the use of such a promising CeO₂ nanostructure to be used at the industrial level for ibuprofen-based pharmaceutical wastewater treatment.

Notation

Abs	Absorbance [AU]
c_i	Concentration of component i [mol/m ³]
Ea_j	Activation energy for reaction j [kJ/mol]
F_{obj}	Objective function [-]
h	Plank constant [m ² .kg/s]
K_B	Boltzmann's constant [m ² .kg/s ² .K]
$k_{ref,j}$	Kinetic constant calculated at a reference temperature [(m ³ /mol)(m ³ /kg ^{n})s ⁻¹]
n	Linearization coefficient for catalyst bulk density [-]
N_{data}	Number of available experimental data [-]
Q_{air}	Air volumetric flowrate [m ³ /s]
r_j	Reaction rate of step j [mol/(kg.s)]
r_{obs}	Observed reaction rate [mol/(m ³ .s)]
R	Ideal gas constant [kJ/(K.mol)]
t	Time [s]
T	Temperature [K]
T_{ref}	Reference temperature, 303K [K]

Greek symbols

ΔG°	Gibbs free energy change [J/mol]
ΔH°	Enthalpy change [J/mol]
ΔS°	Entropy change [J/(mol K)]
v	Stirring rate [rpm]
ρ_B	Catalyst bulk density [kg/m ³]
ρ_{H_2O}	Water density [kg/m ³]

v_{ij} Stoichiometric coefficient of component i in reaction j [-]

Abbreviations

1-OH	1-OH ibuprofen
1-OXO	1-OXO ibuprofen
CALC	Calculated
CI 95%	Confidence intervals calculated at 95%
EXP	Experimental
IBU	Ibuprofen
M	Correlation matrix

Acknowledgments

The authors are grateful to Dr. Rocco Di Girolamo (Department of Chemical Science, University of Naples Federico II) for his support in TEM analysis and to Marica Chianese for her experimental support in conducting the kinetic experiments. The authors also thank CEA-LETI (Grenoble, France) for providing the access to XPS instrument.

Conflict of Interest

The authors declare that the research was conducted in the absence of any commercial or financial relationships that could be construed as a potential conflict of interest.

Author Contributions

Vincenzo Russo and Giuseppe Vitiello wrote the original draft of the manuscript. The main conceptual ideas were drawn from the interactions between Vincenzo Russo and Giuseppe Vitiello, while the funds were obtained by the synergistic effect of the cooperation between Martino Di Serio and Luigi Paduano. The experimental work, the data elaboration, and the formal analysis were

conducted by Noemi Gallucci, Maryam Hmoudah, Amjad El-Qanni, and Eugenie Martinez. The final draft was revised by Giuseppe Vitiello and Vincenzo Russo.

Funding

12th executive program for scientific and technological cooperation between the Italian Republic and the Republic of Korea for the years 2019-2021 is acknowledged for financial support.

This project has received funding from the EU-H2020 research and innovation program under the grant agreement No. 2018.1:677 (ID677) having benefitted from the access provided by CEA-LETI in Grenoble (France) within the framework of the NFFA-Europe Transnational Access Activity.

References

- [1] B. Xu, F. Qi, D. Sun, Z. Chen, D. Robert, Cerium doped red mud catalytic ozonation for bezafibrate degradation in wastewater: Efficiency, intermediates, and toxicity, *Chemosphere* 146 (2016) 22-31. <https://doi.org/https://doi.org/10.1016/j.chemosphere.2015.12.016>.
- [2] A. Kumar, G. Sharma, M. Naushad, A.a.H. Al-Muhtaseb, A. Kumar, I. Hira, T. Ahamad, A.A. Ghfar, F.J. Stadler, Visible photodegradation of ibuprofen and 2,4-D in simulated waste water using sustainable metal free-hybrids based on carbon nitride and biochar, *Journal of Environmental Management* 231 (2019) 1164-1175. <https://doi.org/https://doi.org/10.1016/j.jenvman.2018.11.015>.
- [3] S. Saeid, P. Tolvanen, N. Kumar, K. Eränen, J. Peltonen, M. Peurla, J.-P. Mikkola, A. Franz, T. Salmi, Advanced oxidation process for the removal of ibuprofen from aqueous solution: A non-catalytic and catalytic ozonation study in a semi-batch reactor, *Applied Catalysis B: Environmental* 230 (2018) 77-90. <https://doi.org/https://doi.org/10.1016/j.apcatb.2018.02.021>.
- [4] S.D. Richardson, S.Y. Kimura, *Water Analysis: Emerging Contaminants and Current Issues*, *Analytical Chemistry* 92(1) (2020) 473-505. <https://doi.org/10.1021/acs.analchem.9b05269>.
- [5] L.F.V. Francisco, B. do Amaral Crispim, J.C.V. Spósito, J.C.J. Solórzano, N.H. Maran, F. Kummrow, V.A. do Nascimento, C.C. Montagner, K.M.P. De Oliveira, A. Barufatti, Metals and emerging contaminants in groundwater and human health risk assessment, *Environmental Science and Pollution Research* 26(24) (2019) 24581-24594. <https://doi.org/10.1007/s11356-019-05662-5>.
- [6] B.S. Rathi, P.S. Kumar, P.-L. Show, A review on effective removal of emerging contaminants from aquatic systems: Current trends and scope for further research, *Journal of Hazardous Materials* (2020) 124413. <https://doi.org/https://doi.org/10.1016/j.jhazmat.2020.124413>.
- [7] P.R. Rout, T.C. Zhang, P. Bhunia, R.Y. Surampalli, Treatment technologies for emerging contaminants in wastewater treatment plants: A review, *Science of The Total Environment* 753 (2021) 141990. <https://doi.org/https://doi.org/10.1016/j.scitotenv.2020.141990>.
- [8] H. Chaker, S. Fourmentin, L. Chérif-Aouali, Efficient Photocatalytic Degradation of Ibuprofen under Visible Light Irradiation Using Silver and Cerium Co-Doped Mesoporous TiO₂, *ChemistrySelect* 5(38) (2020) 11787-11796. <https://doi.org/https://doi.org/10.1002/slct.202002730>.
- [9] G. Boczkaj, A. Fernandes, Wastewater treatment by means of advanced oxidation processes at basic pH conditions: A review, *Chemical Engineering Journal* 320 (2017) 608-633. <https://doi.org/https://doi.org/10.1016/j.cej.2017.03.084>.

- [10] A. Gul, N.G. Khaligh, N.M. Julkapli, Surface modification of Carbon-Based Nanoadsorbents for the Advanced Wastewater Treatment, *Journal of Molecular Structure* 1235 (2021) 130148. <https://doi.org/https://doi.org/10.1016/j.molstruc.2021.130148>.
- [11] A. Ahmad, S.H. Mohd-Setapar, C.S. Chuong, A. Khatoon, W.A. Wani, R. Kumar, M. Rafatullah, Recent advances in new generation dye removal technologies: novel search for approaches to reprocess wastewater, *RSC Advances* 5(39) (2015) 30801-30818. <https://doi.org/10.1039/C4RA16959J>.
- [12] I. Gehrke, A. Geiser, A. Somborn-Schulz, Innovations in nanotechnology for water treatment, *Nanotechnology, science and applications* 8 (2015) 1-17. <https://doi.org/10.2147/NSA.S43773>.
- [13] A.S. Adeleye, J.R. Conway, K. Garner, Y. Huang, Y. Su, A.A. Keller, Engineered nanomaterials for water treatment and remediation: Costs, benefits, and applicability, *Chemical Engineering Journal* 286 (2016) 640-662. <https://doi.org/https://doi.org/10.1016/j.cej.2015.10.105>.
- [14] S. Dong, J. Feng, M. Fan, Y. Pi, L. Hu, X. Han, M. Liu, J. Sun, J. Sun, Recent developments in heterogeneous photocatalytic water treatment using visible light-responsive photocatalysts: a review, *RSC Advances* 5(19) (2015) 14610-14630. <https://doi.org/10.1039/C4RA13734E>.
- [15] M.A. Sousa, C. Gonçalves, V.J.P. Vilar, R.A.R. Boaventura, M.F. Alpendurada, Suspended TiO₂-assisted photocatalytic degradation of emerging contaminants in a municipal WWTP effluent using a solar pilot plant with CPCs, *Chemical Engineering Journal* 198-199 (2012) 301-309. <https://doi.org/https://doi.org/10.1016/j.cej.2012.05.060>.
- [16] C. Tortajada, Contributions of recycled wastewater to clean water and sanitation Sustainable Development Goals, *npj Clean Water* 3(1) (2020) 22. <https://doi.org/10.1038/s41545-020-0069-3>.
- [17] M. Vatanparast, L. Saedi, Sonochemical-assisted synthesis and characterization of CeO₂ nanoparticles and its photocatalytic properties, *Journal of Materials Science: Materials in Electronics* 29(9) (2018) 7107-7113. <https://doi.org/10.1007/s10854-018-8698-8>.
- [18] S. Yuán, B. Xu, Q. Zhang, S. Liu, J. Xie, M. Zhang, T. Ohno, Development of the Visible-Light Response of CeO_{2-x} with a high Ce³⁺ Content and Its Photocatalytic Properties, *ChemCatChem* 10(6) (2018) 1267-1271. <https://doi.org/https://doi.org/10.1002/cctc.201701767>.
- [19] L. Gnanasekaran, R. Hemamalini, R. Saravanan, K. Ravichandran, F. Gracia, S. Agarwal, V.K. Gupta, Synthesis and characterization of metal oxides (CeO₂, CuO, NiO, Mn₃O₄, SnO₂ and ZnO) nanoparticles as photo catalysts for degradation of textile dyes, *Journal of Photochemistry and Photobiology B: Biology* 173 (2017) 43-49. <https://doi.org/https://doi.org/10.1016/j.jphotobiol.2017.05.027>.
- [20] M. Aslam, M.T. Qamar, M.T. Soomro, I.M.I. Ismail, N. Salah, T. Almeelbi, M.A. Gondal, A. Hameed, The effect of sunlight induced surface defects on the photocatalytic activity of nanosized CeO₂ for the degradation of phenol and its derivatives, *Applied Catalysis B: Environmental* 180 (2016) 391-402. <https://doi.org/https://doi.org/10.1016/j.apcatb.2015.06.050>.
- [21] P. Borker, A.V. Salker, Solar assisted photocatalytic degradation of Naphthol Blue Black dye using Ce_{1-x}Mn_xO₂, *Materials Chemistry and Physics* 103(2) (2007) 366-370. <https://doi.org/https://doi.org/10.1016/j.matchemphys.2007.02.034>.
- [22] D. Majumder, I. Chakraborty, K. Mandal, S. Roy, Facet-Dependent Photodegradation of Methylene Blue Using Pristine CeO₂ Nanostructures, *ACS Omega* 4(2) (2019) 4243-4251. <https://doi.org/10.1021/acsomega.8b03298>.
- [23] F. Naaz, U. Farooq, T. Ahmad, Ceria as an Efficient Nanocatalyst for Organic Transformations, *Nanocatalysts*, IntechOpen2019. <https://doi.org/10.5772/intechopen.82688>.
- [24] J.A. Rodriguez, D.C. Grinter, Z. Liu, R.M. Palomino, S.D. Senanayake, Ceria-based model catalysts: fundamental studies on the importance of the metal-ceria interface in CO oxidation, the water-gas shift, CO₂ hydrogenation, and methane and alcohol reforming, *Chemical Society Reviews* 46(7) (2017) 1824-1841. <https://doi.org/10.1039/C6CS00863A>.
- [25] C. Maria Magdalane, K. Kaviyarasu, A. Raja, M.V. Arularasu, G.T. Mola, A.B. Isaev, N.A. Al-Dhabi, M.V. Arasu, B. Jeyaraj, J. Kennedy, M. Maaza, Photocatalytic decomposition effect of erbium doped cerium oxide nanostructures driven by visible light irradiation: Investigation of

- cytotoxicity, antibacterial growth inhibition using catalyst, *Journal of Photochemistry and Photobiology B: Biology* 185 (2018) 275-282. <https://doi.org/https://doi.org/10.1016/j.jphotobiol.2018.06.011>.
- [26] S.M.M. (SMM), SMM Spot prices. <https://www.metal.com/>. (Accessed June 3rd 2021).
- [27] A.S. Weber, A.M. Grady, R.T. Koodali, Lanthanide modified semiconductor photocatalysts, *Catalysis Science & Technology* 2(4) (2012) 683-693. <https://doi.org/10.1039/C2CY00552B>.
- [28] M.E. Kibar, Preparation of copper oxide-cerium oxide/nanotube-titanium dioxide photocatalyst for CO₂ conversion in solar light, *Reaction Kinetics, Mechanisms and Catalysis* 134(2) (2021) 937-950. <https://doi.org/10.1007/s11144-021-02079-5>.
- [29] Y.-C. Zhang, Z. Li, L. Zhang, L. Pan, X. Zhang, L. Wang, A. Fazal e, J.-J. Zou, Role of oxygen vacancies in photocatalytic water oxidation on ceria oxide: Experiment and DFT studies, *Applied Catalysis B: Environmental* 224 (2018) 101-108. <https://doi.org/https://doi.org/10.1016/j.apcatb.2017.10.049>.
- [30] M.M. Khan, S.A. Ansari, D. Pradhan, D.H. Han, J. Lee, M.H. Cho, Defect-Induced Band Gap Narrowed CeO₂ Nanostructures for Visible Light Activities, *Industrial & Engineering Chemistry Research* 53(23) (2014) 9754-9763. <https://doi.org/10.1021/ie500986n>.
- [31] G. Jayakumar, A. Albert Irudayaraj, A. Dhayal Raj, Particle Size Effect on the Properties of Cerium Oxide (CeO₂) Nanoparticles Synthesized by Hydrothermal Method, *Mechanics, Materials Science & Engineering Journal* 9(1) (2017). <https://doi.org/10.2412/mmse.3.4.481>.
- [32] B. Choudhury, A. Choudhury, Ce³⁺ and oxygen vacancy mediated tuning of structural and optical properties of CeO₂ nanoparticles, *Materials Chemistry and Physics* 131(3) (2012) 666-671. <https://doi.org/https://doi.org/10.1016/j.matchemphys.2011.10.032>.
- [33] C. Yang, X. Yu, P.N. Pleßow, S. Heißler, P.G. Weidler, A. Nefedov, F. Studt, Y. Wang, C. Wöll, Rendering Photoreactivity to Ceria: The Role of Defects, *Angewandte Chemie International Edition* 56(45) (2017) 14301-14305. <https://doi.org/https://doi.org/10.1002/anie.201707965>.
- [34] J.K. Sharma, P. Srivastava, S. Ameen, M.S. Akhtar, S.K. Sengupta, G. Singh, Phytoconstituents assisted green synthesis of cerium oxide nanoparticles for thermal decomposition and dye remediation, *Materials Research Bulletin* 91 (2017) 98-107. <https://doi.org/https://doi.org/10.1016/j.materresbull.2017.03.034>.
- [35] P. Latha, K. Prakash, S. Karuthapandian, Effective Photodegradation of CR & MO dyes by morphologically controlled Cerium oxide nanocubes under visible light Illumination, *Optik* 154 (2018) 242-250. <https://doi.org/https://doi.org/10.1016/j.ijleo.2017.10.054>.
- [36] S. Sehar, I. Naz, A. Rehman, W. Sun, S.S. Alhewairini, M.N. Zahid, A. Younis, Shape-controlled synthesis of cerium oxide nanoparticles for efficient dye photodegradation and antibacterial activities, *Applied Organometallic Chemistry* 35(1) (2021) e6069. <https://doi.org/https://doi.org/10.1002/aoc.6069>.
- [37] S.J. Saadon, M. Jarosova, P. Machek, M.M. Kadhim, M.H. Ali, A.D. Khalaji, Methylene blue photodegradation using as-synthesized CeO₂ nanoparticles, *Journal of the Chinese Chemical Society* n/a(n/a) (2021). <https://doi.org/https://doi.org/10.1002/jccs.202100476>.
- [38] N.M. Lopés-Velasco, S.J. Bailón-Ruiz, Effect of the particle size and pH on the photocatalytic performance of cerium oxide (CeO₂) nanoparticles, *MRS Advances* 6(32) (2021) 769-773. <https://doi.org/10.1557/s43580-021-00070-9>.
- [39] A.I.Y. Tok, F.Y.C. Boey, Z. Dong, X.L. Sun, Hydrothermal synthesis of CeO₂ nano-particles, *Journal of Materials Processing Technology* 190(1) (2007) 217-222. <https://doi.org/https://doi.org/10.1016/j.jmatprotec.2007.02.042>.
- [40] E.P. Barrett, L.G. Joyner, P.P. Halenda, The Determination of Pore Volume and Area Distributions in Porous Substances. I. Computations from Nitrogen Isotherms, *Journal of the American Chemical Society* 73(1) (1951) 373-380. <https://doi.org/10.1021/ja01145a126>.
- [41] D. Girija, H.S.B. Naik, C. Sudhamani, B.V. Kumar, Cerium Oxide Nanoparticles—A Green, Reusable, and Highly Efficient Heterogeneous Catalyst for the Synthesis of Polyhydroquinolines under Solvent-Free Conditions, *Archives of Applied Science Research* 3(3) (2011) 373-382.

- [42] M. Okuda, Y. Suzumoto, I. Yamashita, Bioinspired Synthesis of Homogenous Cerium Oxide Nanoparticles and Two- or Three-Dimensional Nanoparticle Arrays Using Protein Supramolecules, *Crystal Growth & Design* 11(6) (2011) 2540-2545. <https://doi.org/10.1021/cg200299y>.
- [43] E. Kusmierek, A CeO₂ Semiconductor as a Photocatalytic and Photoelectrocatalytic Material for the Remediation of Pollutants in Industrial Wastewater: A Review, *Catalysts* 10(12) (2020). <https://doi.org/10.3390/catal10121435>.
- [44] M. Kråkström, S. Saeid, P. Tolvanen, N. Kumar, T. Salmi, L. Kronberg, P. Eklund, Identification and Quantification of Transformation Products Formed during the Ozonation of the Non-steroidal Anti-inflammatory Pharmaceuticals Ibuprofen and Diclofenac, *Ozone: Science & Engineering* (2021) 1-15. <https://doi.org/10.1080/01919512.2021.1898928>.
- [45] S. Saeid, M. Kråkström, P. Tolvanen, N. Kumar, K. Eränen, M. Peurla, J.-P. Mikkola, L. Maël, L. Kronberg, P. Eklund, T. Salmi, Synthesis and Characterization of Metal Modified Catalysts for Decomposition of Ibuprofen from Aqueous Solutions, *Catalysts* 10(7) (2020). <https://doi.org/10.3390/catal10070786>.
- [46] K. Byrappa, A.K. Subramani, S. Ananda, K.M.L. Rai, R. Dinesh, M. Yoshimura, Photocatalytic degradation of rhodamine B dye using hydrothermally synthesized ZnO, *Bulletin of Materials Science* 29(5) (2006) 433-438. <https://doi.org/10.1007/BF02914073>.
- [47] M. Rezaei, A. Nezamzadeh-Ejhieha, The ZnO-NiO nano-composite: A brief characterization, kinetic and thermodynamic study and study the Arrhenius model on the sulfasalazine photodegradation, *International Journal of Hydrogen Energy* 45(46) (2020) 24749-24764. <https://doi.org/https://doi.org/10.1016/j.ijhydene.2020.06.258>.
- [48] A.S.M. Kuba, A.M.J.A.L. Shamari, Kinetics and thermodynamics study for photodegradation of Brown HT dye by MnO and NiO as catalysis, *Materials Today: Proceedings* 49 (2022) 2741-2746. <https://doi.org/https://doi.org/10.1016/j.matpr.2021.09.256>.